processes

MDPI

Article

Study on the Effect of Bubbles on the Removal Efficiency of a Helical Tube Flocculator

Yiming Zhang [1], Chuanzhen Wang [1], Md. Shakhaoath Khan [2,*], Xuezhi Zhang [3], Zihao Wang [4], Buqing Yang [5] and Haiyang Zhang [3,*]

[1] China Anhui Engineering Research Center for Coal Clean Processing and Carbon Reduction, College of Material Science and Engineering, Anhui University of Science and Technology, Huainan 232001, China; 2022201064@aust.edu.cn (Y.Z.); faxofking@aust.edu.cn (C.W.)
[2] Department of Chemical Engineering, Monash University, Clayton, VIC 3800, Australia
[3] Institute of Hydrobiology, Chinese Academy of Sciences, Wuhan 430072, China; zhangxuezhi@ihb.ac.cn
[4] Bgrimm Technology Group, Beijing 100260, China; 17788376963@163.com
[5] Computer Science and Technology, College of Computer Engineering, Tongda College of Nanjing University of Posts and Telecommunications, Yangzhou 210037, China; 13921399516@163.com
* Correspondence: ms.khan@monash.edu (M.S.K.); hyzhang@ihb.ac.cn (H.Z.); Tel.: +61-(3)-9905-6003 (M.S.K.); +86-2768780929 (H.Z.)

Abstract: The tubular flocculation reactor is a new and efficient device for treating algae-containing wastewater. The introduction of bubbles during the reaction process can effectively shorten the time required for floc separation. However, the impact of bubbles on floc formation and removal in the tubular flocculation reactor is not well understood. To further clarify the effect of bubbles on the reactor's operation, this study employed a uniform experimental design, varying the flow rate, chemical dosage, bubble reaction distance, and bubble injection rate in the reactor to examine the influence of bubbles under different operating conditions. The results indicated that as the bubble reaction distance increased from 0 m to 7.6 m, the removal efficiency increased from 60% to 70%, the floc size increased from 160 μm to 165 μm, and the fractal dimension decreased from 2.1 to 1.9. When the bubble volume increased from 5% to 30%, the removal efficiency increased from 50% to 80%. Under constant bubble conditions, the rising speed of the flocs increased from 0.4 mm·s^{-1} to 1.2 mm·s^{-1}, while the removal efficiency increased from 30% to 90%. A logarithmic correlation was observed between the rising speed and removal efficiency. A linear relationship was found between the floc rising speed and the floc size, with floc size increasing from 200 μm to 800 μm and the rising speed increasing from 0.4 mm·s^{-1} to 2.3 mm·s^{-1}. An exponential relationship was found between the fractal dimension and the rising speed, with the rising speed decreasing from 2.3 mm·s^{-1} to 0.4 mm·s^{-1}, while the fractal dimension increased from 1.93 to 2.02.

Keywords: tubular flocculation reactor; bubbles; floc morphology; floc rising speed; removal efficiency

check for updates

Academic Editors: Alejandro Regalado-Méndez, Reyna Natividad and Rubi Romero

Received: 22 January 2025
Revised: 28 February 2025
Accepted: 3 March 2025
Published: 6 March 2025

Citation: Zhang, Y.; Wang, C.; Khan, M.S.; Zhang, X.; Wang, Z.; Yang, B.; Zhang, H. Study on the Effect of Bubbles on the Removal Efficiency of a Helical Tube Flocculator. *Processes* **2025**, *13*, 758. https://doi.org/10.3390/pr13030758

Copyright: © 2025 by the authors. Licensee MDPI, Basel, Switzerland. This article is an open access article distributed under the terms and conditions of the Creative Commons Attribution (CC BY) license (https://creativecommons.org/licenses/by/4.0/).

1. Introduction

Under the background of global warming, the rapid development of socio-economic activities has exacerbated the issue of water eutrophication [1], significantly increasing the likelihood of harmful algal blooms in rivers, lakes, and reservoirs [2]. The outbreak of harmful algal blooms can severely damage the health of aquatic ecosystems [3], leading to the death of aquatic organisms such as fish and shrimp [4] and causing lakes to shift from clear waters dominated by large aquatic plants to turbid waters dominated by algae,

thus resulting in a gradual decline in water quality [5]. Harmful algal blooms typically generate large amounts of algal toxins and odorous substances [6], threatening the safety of drinking water for the general public [7]. Although the most effective strategy for addressing harmful algal blooms is ecological restoration [8], which involves reducing nutrients in water bodies and rebuilding healthy aquatic ecosystems [9], this process may take years or even decades to achieve [10]. Therefore, immediate remedial measures are urgently needed for water bodies currently affected by harmful algal blooms [11] in order to mitigate the adverse effects on the health of aquatic ecosystems and drinking water safety [12].

Among various emergency control measures for harmful algal blooms, algae harvesting—i.e., separating algae from water—is considered one of the most feasible methods and has been widely applied in water bodies affected by harmful algal blooms [13]. Algae harvesting can quickly reduce algal biomass in the water [14], preventing large-scale algal die-offs and minimizing damage to aquatic ecosystems [15]. Furthermore, removing algae biomass also allows for the extraction of large amounts of nutrients, such as nitrogen and phosphorus [16]. In addition, during the summer, algae are the main suspended particles in drinking water sources [17], making algae-water separation an essential step in the water treatment process [18]. Currently, the most commonly used technologies for algae-water separation include coagulation-sedimentation [19], coagulation-flotation [20], and coagulation-filtration [21]. A common feature of these technologies is that they initially cause algae cells to aggregate into flocs, improving the efficiency of algae-water separation [22]. Therefore, forming algae flocs suitable for separation is a prerequisite for achieving optimal algae-water separation efficiency [23].

Research has shown that under different hydraulic conditions, the settling performance of algae flocs differs significantly [24], and only under appropriate hydraulic conditions can large and dense algae flocs be formed to achieve the best settling performance [25]. Similar conclusions have been drawn for algae-water separation via flotation methods [26]. Specifically, the structure of algae flocs, controlled by hydraulic shear forces (such as stirring speed), plays a critical role [27]. Larger and denser flocs are more likely to attach to microbubbles [28], and during the flotation process, they can better resist hydraulic disturbances [29], leading to more efficient and faster separation [30]. The tubular flocculator is a novel floc formation system that, compared to traditional mechanical stirring flocculators [31], has advantages such as simpler structure, no need for additional energy input, and shorter residence time [32]. Research by Professor Haiyang Zhang has shown that flocs formed in tubular flocculators settle or rise faster than those formed by mechanical stirring. Our previous research has also found that the algal flocs produced by the tubular flocculator are more compact, with a more ideal rising velocity, and require less coagulant, saving more than 50% of the chemical dosage.

To further enhance the removal efficiency of tubular reactors, bubbles are introduced into the tubular coagulation reactor to accelerate the rising speed of flocs. This study uses a uniform experimental design to compare the effects of bubbles on floc formation under different tube lengths and bubble water ratios. The morphology and rising speed of the flocs are statistically generated by varying flow rates and coagulant concentrations. The aims of this study are to clarify the relationship between rising speed and floc characteristics and to compare the relationship between removal efficiency and rising speed to determine the impact of bubbles on removal efficiency.

2. Materials and Methods

2.1. Experimental Design

As shown in Figure 1, the experimental schematic diagram illustrates the impact of introducing bubbles into the tubular coagulation reactor on floc formation. The experiment involves three peristaltic pumps to introduce coagulants and samples. The coagulants selected are polyaluminum chloride (PAC) and polyacrylamide (PAM). A dissolved air tank is used to generate pressurized dissolved air–water, which is then introduced into the tubular flocculation reactor's inlet, where it mixes with the sample and coagulants before entering the reactor. Bubbles are released in the spiral tube reactor and participate in the floc formation process.

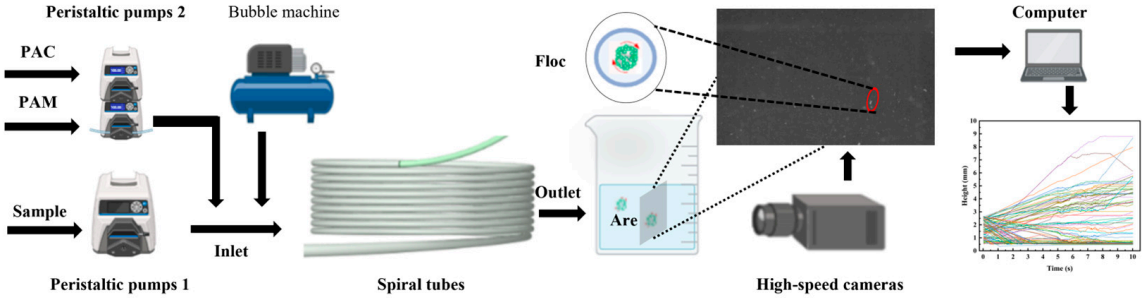


Figure 1. Schematic diagram of the study on the effect of bubbles on the removal efficiency of the reactor.

After the reaction, the sample is collected from the outlet of the spiral tube reactor into a square container (50 × 150 × 5 mm). One end of the container is painted black, while the other end is illuminated. A high-speed camera is used to record a 10-s video capturing 40,000 frames for post-processing to obtain parameters such as floc shape and rising speed. Two types of spiral tube reactors were used, with a helix central radius of 100 mm and a pipe spacing of 1 mm, made from PVC pipes with diameters of 12 mm and 6 mm, respectively. The equipment parameters are shown in Table 1.

Table 1. Equipment and coagulants used.

Project	Specification
Diaphragm pumps 1	0.2–5 L·min^{-1}
Diaphragm pumps 2	0.1–0.7 mL·s^{-1}
Spectrophotometer	DR6000, HACH, USA
High-speed camera	EO-410 L, Phantom, USA
Spiral tubes length	6700 mm
Spiral tubes radius	100 mm
Spiral tubes inner diameter	12 mm, 6 mm
Bubble machine	GWNB1, Gongyuan, China

The experiment was conducted using a halloysite nanoclay suspension, with the clay being kaolinite with a particle size of 0.1 μm. The concentration of the solution was characterized by measuring the absorbance at a wavelength of 680 nm using a spectrophotometer. The experiment was mainly divided into two stages: the preparation stage and the formal experimental stage.

In the preparation stage, the halloysite nanoclay suspension, reagents, and air–water were mainly prepared. The reagents and halloysite nanoclay suspension were prepared using laboratory secondary pure water, and the air–water was prepared using clear water. The pH value of the pure water was 6.71, TOD was 1.2 mg·L^{-1}, and the conductivity was 2.3 μS·cm^{-1}.

To achieve the required linear velocity, the equipment had a large processing capacity. To avoid experimental interruptions leading to significant fluctuations in the conclusions of a set of experiments, the halloysite nanoclay suspension was prepared by diluting a high-concentration solution. To shorten the dispersion time of the suspension and improve the stability of the suspension, the high-concentration solution was prepared using pure water. During the preparation process, a stirrer was used to stir at a speed of 700 r·min^{-1} under standard atmospheric pressure at 25 °C for at least 8 h. The concentration of the high-concentration solution was 5 g·L^{-1}, and the Zeta potential of the kaolinite colloid was −40.9 mV at this time.

To avoid changes in the properties of the reagents, the reagents were prepared using pure water. PAC and PAM were baked in a 60 °C oven for 3 h, and then 5 g of each was weighed using an electronic balance and dissolved in 5 L of pure water to prepare two bottles of solutions with a concentration of 1 g·L^{-1} for standby use, with PAM needing to be stirred at a speed of 300 r·min^{-1} under standard atmospheric pressure at 25 °C for more than 3 h.

In the pressure vessel, clear water was filled to one-third of its capacity, and air was pumped in using an air pump to reach 0.8 MPa. The pressure vessel was left undisturbed for more than half an hour to ensure the stability of the air–water. After air dissolution, a 10 mL water sample was taken and left undisturbed until the bubbles disappeared. The absorbance was measured at a wavelength of 680 nm using a spectrophotometer, and the sample was tested three times with the average value taken as the absorbance D_2 of the air–water.

Before the formal experiment, the high-concentration halloysite nanoclay suspension was diluted to the required concentration D_0 using clear water. During the experiment, continuous stirring was needed to ensure the uniform dispersion of kaolinite in the suspension and to maintain the stability of the pressure in the air–water container to avoid fluctuations in flow rate and air content. The specific experimental steps were as follows:

(1) The samples, reagents, and bubbly water were introduced into the inlet of the helical reactor at a constant rate. The samples and reagents were pumped in using peristaltic pumps, with the reagents being PAC and PAM. The flow rate of the bubbly water was controlled by adjusting the valve size.

(2) Liquids were directly introduced into the helical reactor. After the reaction in the reactor, two 500 mL cups of solution were collected at the outlet using beakers. Immediately, a high-speed camera was used to film for 10 s at a frame rate of 4000 fps. After the filming, the setup was left undisturbed.

(3) After standing for 5 min, 10 mL of the solution was taken from 3 cm below the surface of the liquid in the beaker. Absorbance was measured at 680 nm using a spectrophotometer. Each sample was tested three times, and the average value was taken to determine the concentration after removal D_3.

(4) The removal efficiency was calculated, and the effect of dissolved air–water was subtracted using the following formula, where D_0 is the initial absorbance, D_2 is the absorbance of the dissolved air–water, α_2 is the proportion of dissolved air introduced, and D_3 is the absorbance of the liquid sampled using a pipette.

$$(D_0 - (\frac{D_3 - D_2\alpha_2}{1 - \alpha_2}))/D_0 \quad (1)$$

The experiment used a uniform experimental design. During the experiment, parameters such as sample concentration, flow rate in the pipe, coagulant concentration, pipe diameter, pipe length, and the proportion of dissolved air–water were varied. The detailed

parameters are shown in Table 2. The dose of coagulants and the flow rate of the fluid in the pipe were controlled by adjusting the pumping speed of the peristaltic pump.

Table 2. Experimental parameters.

Item	Parameter
Concentration of sample ($g \cdot L^{-1}$)	0.05, 0.1, 0.15, 0.2, 0.25, 0.3
Concentration of PAC ($mg \cdot L^{-1}$)	0.5, 1, 1.5, 2
Concentration of PAM ($mg \cdot L^{-1}$)	0.5, 1, 1.5, 2
Velocity of sample ($m \cdot s^{-1}$)	0.15, 0.2, 0.25, 0.3
Bubble participation length (m)	6.7, 6, 5.5, 5, 4.5, 4, 3.5, 3, 2.5, 2, 1.5, 1
Pipe diameter (mm)	6, 12
Bubble ratio of sample	0.1, 0.15, 0.2, 0.25

2.2. Video Processing Method

The video processing method is shown in Figure 2. The processing process mainly consists of two parts: floc recognition and tracking. In the floc recognition step, the initial position, size, and fractal dimension of the flocs are obtained; in the tracking step, the movement of the flocs is followed to determine their rising velocity. The specific processing steps are as follows:

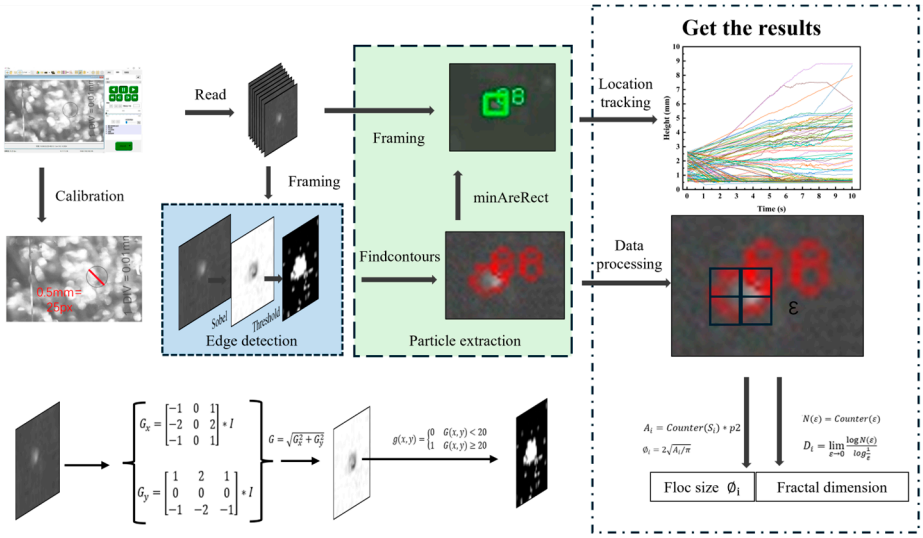


Figure 2. Schematic diagram of video processing.

(1) Calibration: Before filming, the focal length of the lens was adjusted until the particles were clearly visible. A ruler of known length was placed in the filming window. Using the software ImageJ (1.8.0), the number of pixels corresponding to the unit length of the ruler was measured [33], obtaining the length-to-pixel relationship p, with a result of 20 $\mu m \cdot px^{-1}$.

(2) Framing: The video recorded by the high-speed camera was stored in cine format with a frame rate of 4000 fps. Post-processing was carried out using Python (3.12.4) and the OpenCV library (4.10.0) to write a recognition program. Every 100th frame from the first 40,000 frames of the video was processed. An if function was used to determine if the frame number was divisible by 100 to extract the frames that needed to be processed. The extracted frames were then subjected to recognition and tracking.

(3) Processing the image frames: The processing of the obtained image frames includes two parts: edge detection and particle extraction. The specific operations are as follows:

Edge detection: The images obtained from framing were processed using the Sobel operator to detect the particle edges in the images. The algorithm is implemented through the following calculation:

$$G_x = \begin{bmatrix} -1 & 0 & 1 \\ -2 & 0 & 2 \\ -1 & 0 & 1 \end{bmatrix} * I, \quad G_y = \begin{bmatrix} 1 & 2 & 1 \\ 0 & 0 & 0 \\ -1 & -2 & -1 \end{bmatrix} * I \tag{2}$$

The Sobel operator is an algorithm that identifies the edges of particles in an image by calculating the rate of change of the grayscale values in a grayscale image. Here, I represents the input video image, and G_x and G_y are the feature values of the image in the x and y axes, respectively. G_x and G_y are then transformed and combined into a grayscale image G, which is subsequently binarized to g(x,y) for edge detection of the particles. This step is implemented through the following calculations:

$$G = \sqrt{G_x^2 + G_y^2}, \quad g(x,y) = \begin{cases} 0 & G(x,y) < 20 \\ 1 & G(x,y) \geq 20 \end{cases} \tag{3}$$

Particle extraction: The function FindContours is used to detect closed regions enclosed by parameter 1 in g(x,y). In addition to the image information, the function requires two parameters: "independent contours" and "only count the outermost layer".

The FindContours function traverses the binarized grayscale image, examining all pixels that meet the given value. Starting from the first point, it checks for adjacent points until closure and includes each detected pixel in an array. After all pixels with the given value in the image have been traversed, an array S is output, which contains all closed regions and their corresponding pixels. Each closed region corresponding to a particle is denoted as S_i.

The minAreaRect function is then applied to each S_i to obtain the corresponding minimum enclosing rectangle W_i, and all W_i are stored in an array W.

(4) Get the results: The two arrays, S and W, extracted from the video, are processed. The processing of the S array will yield two parameters related to the floc: size and fractal dimension. The W array will serve as the input file for the dlib library to process the positional information of each floc over time. The detailed calculations are as follows:

Processing of array S: Each closed region S_i within array S is analyzed individually. The number of pixels contained within S_i is counted, and the corresponding area A_i is obtained by using the length-to-pixel relationship p. The floc size $\varnothing_i$ is then calculated using the following formula:

$$\begin{cases} A_i = Counter(S_i) * p^2 \\ \varnothing_i = 2\sqrt{A_i/\pi} \end{cases} \tag{4}$$

The calculation of the fractal dimension is performed using the following formula:

$$\begin{cases} N(\varepsilon) = Counter(\varepsilon) \\ D_i = \lim\limits_{\varepsilon \to 0} \frac{\log N(\varepsilon)}{log\frac{1}{\varepsilon}} \end{cases} \tag{5}$$

where D_i is the fractal dimension of particle i, $N(\varepsilon)$ is the number of squares required to cover the particle region, and ε is the side length of the corresponding squares. $N(\varepsilon)$ is obtained by the filling method, starting from the left side of the closed region and filling squares until no more squares contain pixels from the closed region, then counting the number of squares. An iterative method is used to approach the solution as ε approaches

0, with an initial value of ε being half of the particle size and a scaling factor of 0.8. After performing 10 scales of ε, a linear fit is applied to the calculated $\log \frac{1}{\varepsilon}$ and $\log N(\varepsilon)$, and the slope is taken as D_i.

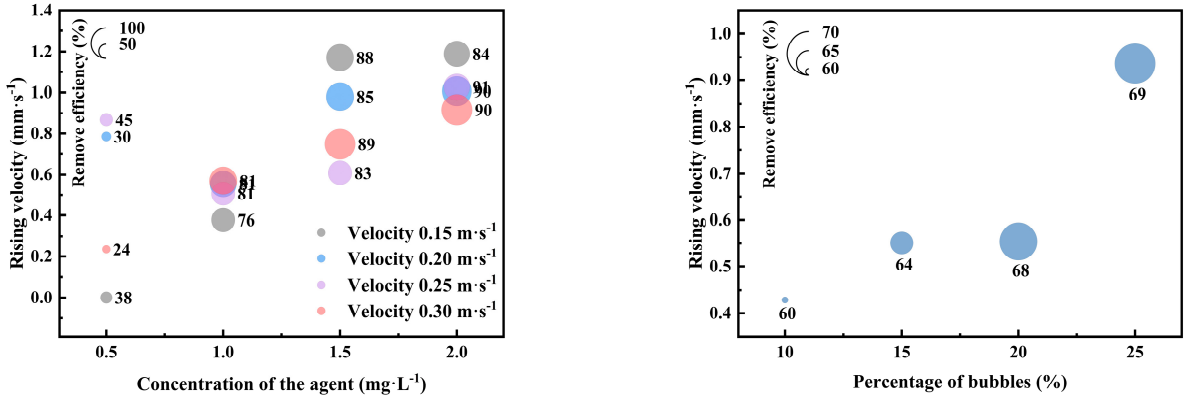
Processing of array W: The video and W array are imported into dlib. For each W_i, an update is performed every 100 frames, and the coordinates of the center point of the tracked bounding box (x_i,y_i) are exported. The value y_i is scaled using p to obtain the height h_i of particle iii at the current time. The time t is calculated using the current frame number and the frame rate.

(5) Data export: The data, including particle number iii, fractal dimension D_i, particle size $\varnothing_i$, time t, and corresponding height h_i, is exported to an Excel file.

3. Results and Discussion

3.1. The Effect of Rising Velocity on Removal Efficiency

As shown in Figure 3, the relationship between removal efficiency and floc rising velocity is illustrated in the bubble chart. Figure 3A shows the bubble chart of floc rising velocity and removal efficiency at a fixed 20% bubble water ratio under different flow rates and coagulant dosages. It can be observed that, when the bubble water ratio is fixed at 20%, increasing the coagulant dosage results in an increase in the floc rising velocity from 0.4 mm·s^{-1} to 1.2 mm·s^{-1}, while the removal efficiency increases from 30% to 90%. Figure 3B displays the bubble chart of floc rising velocity and removal efficiency at different bubble volumes, where the coagulant dosage is fixed at 1.0 mg·L^{-1}, and the flow rate is 0.2 m·s^{-1}. It can be seen that increasing the bubble water inflow ratio leads to an increase in the floc rising velocity from 0.4 mm·s^{-1} to 1 mm·s^{-1}, while the removal efficiency increases from 60% to 69%.



(**A**) (**B**)

Figure 3. Bubble chart of the relationship between removal efficiency and floc rising velocity. (**A**) Bubble chart of floc rising velocity and removal efficiency at different flow rates and coagulant dosages. (**B**) Bubble chart of floc rising velocity and removal efficiency at different bubble volumes.

This is because the kaolinite suspension contains surface charges, and the addition of coagulant PAC reduces the surface charge, thereby promoting floc formation [34] and reducing the concentration of suspended kaolinite. During the coagulation process in the reactor, bubbles contact and attach to the flocs. Increasing the bubble volume leads to more bubbles interacting with the flocs, which are then buoyed by the bubbles, ultimately increasing the removal efficiency [35].

As shown in Figure 3, the variation in removal efficiency indicates a correlation between floc rising velocity and removal efficiency. The fitting result between rising velocity and removal efficiency is shown in Figure 4. It can be observed that as the rising

velocity increases, the removal efficiency increases from 38% to 90%. The rising velocity and removal efficiency follow a logarithmic relationship, with a threshold rising velocity of 0.6 mm·s^{-1}. When the rising velocity exceeds 0.6 mm·s^{-1}, the increase in removal efficiency converges at 90%.

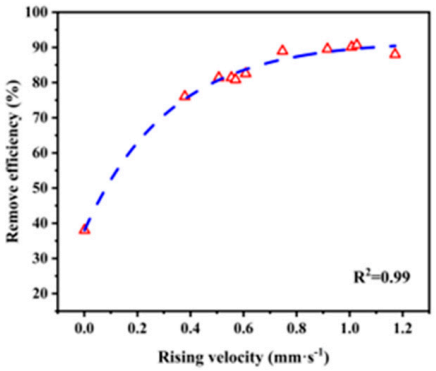


Figure 4. Rising velocity and removal efficiency fitting plot.

3.2. Effect of Floc Shape on Rising Velocity

Figure 5 illustrates the relationship between floc shape and rising velocity. Figure 5A shows the scatter plot of floc size and fractal dimension. It can be observed that as the particle size increases from 200 μm to 800 μm, the fractal dimension of the flocs decreases rapidly from 2.01 to 1.93, indicating a decrease in floc compactness. Before reaching 500 μm, the fractal dimension decreases gradually, but after 500 μm, the decline becomes more rapid.

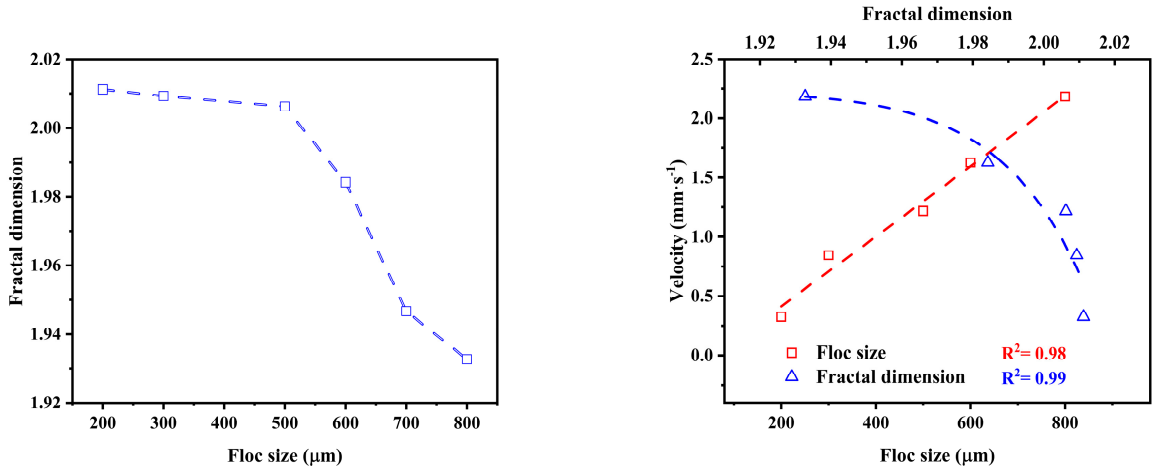


Figure 5. Schematic diagram of the relationship between floc shape and rising velocity. (**A**) Relationship between floc size and fractal dimension. (**B**) Fitting diagram of rising velocity with floc size and fractal dimension.

Figure 5B presents the fitting chart of rising velocity with floc size and fractal dimension. It is evident that the rising velocity of the flocs is linearly related to floc size; as the floc size increases from 200 μm to 800 μm, the rising velocity increases from 0.4 mm·s^{-1} to 2.3 mm·s^{-1}. The rising velocity of the flocs is exponentially related to the fractal dimension. As the fractal dimension increases from 1.93 to 2.02, the rising velocity decreases from 2.3 mm·s^{-1} to 0.4 mm·s^{-1}. This may be because, as the floc size increases, the number of bubbles required for rising increases, and more attachment points are needed for the bubbles. Loose flocs can provide enough attachment points for this process [36].

3.3. The Effect of Bubbles on Floc Formation

Figure 6 is a schematic diagram illustrating the impact of pipe diameter and flow velocity on removal efficiency. It can be observed that there is a significant difference in removal efficiency between the 6 mm and 12 mm pipe diameters, with the 12 mm diameter exhibiting a much higher removal efficiency than the 6 mm one. Considering the subtle differences in flow field conditions within reactors of different diameters, to avoid bias in analyzing the effect of bubbles on floc formation due to variations in shear forces, the following analysis will focus solely on the floc conditions in the 12 mm diameter reactor [37].

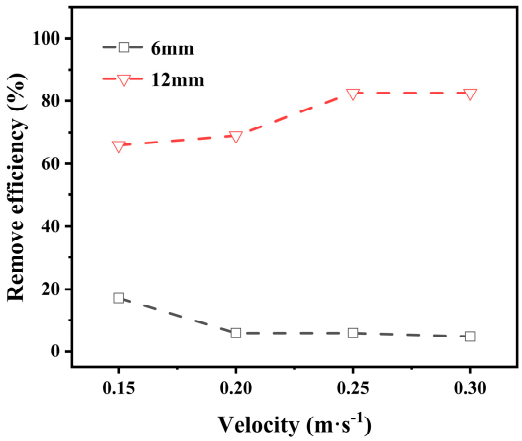


Figure 6. Schematic diagram of the impact of pipe diameter and flow velocity on removal efficiency.

Figure 7 illustrates the effect of the bubble water injection position on removal efficiency. Figure 7A shows the influence of bubble water injection position on floc size and fractal dimension. The *X*-axis represents 0 m for the reactor inlet and 6.7 m for the reactor outlet. It can be observed that as the bubble water injection position moves toward the inlet [38], the reaction time of the bubble water decreases, and the floc size increases from the 160 μm range to 165 μm. As the floc size increases, the fractal dimension decreases from 2.1 to 1.9, indicating that the flocs become looser.

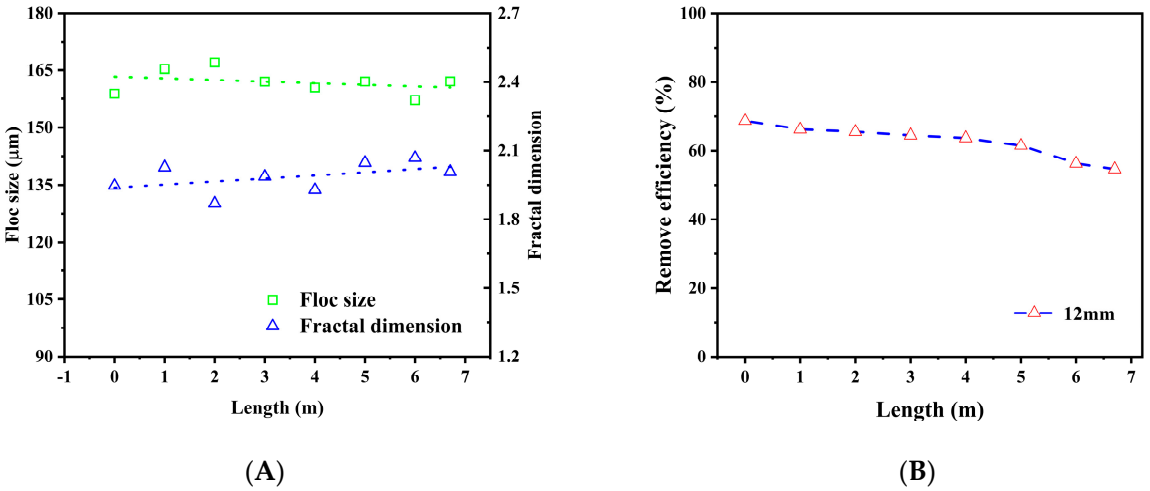


Figure 7. Schematic diagram of the effect of bubble water injection position on removal efficiency. (**A**) Schematic diagram of the effect of bubble water injection position on floc size and fractal dimension. (**B**) Effect of bubble water injection position on removal efficiency.

Figure 7B presents the effect of the bubble water injection position on removal efficiency. As the injection position moves toward the outlet, the removal efficiency gradually decreases. Combined with the results shown in Figure 7A, it can be concluded that as the participation time of bubble water increases, the floc size increases, the compactness of the flocs decreases, and the removal efficiency increases [39]. This suggests that a portion of the bubbles is encapsulated within the flocs.

The effect of the bubble water injection ratio on removal efficiency is shown in Figure 8. It can be observed that as the bubble water injection ratio increases from 5% to 30%, the removal efficiency increases from 50% to over 80%.

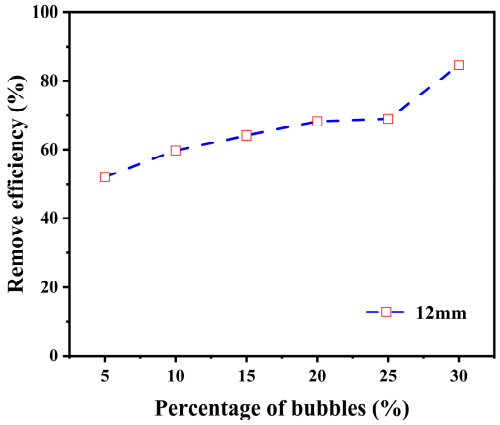
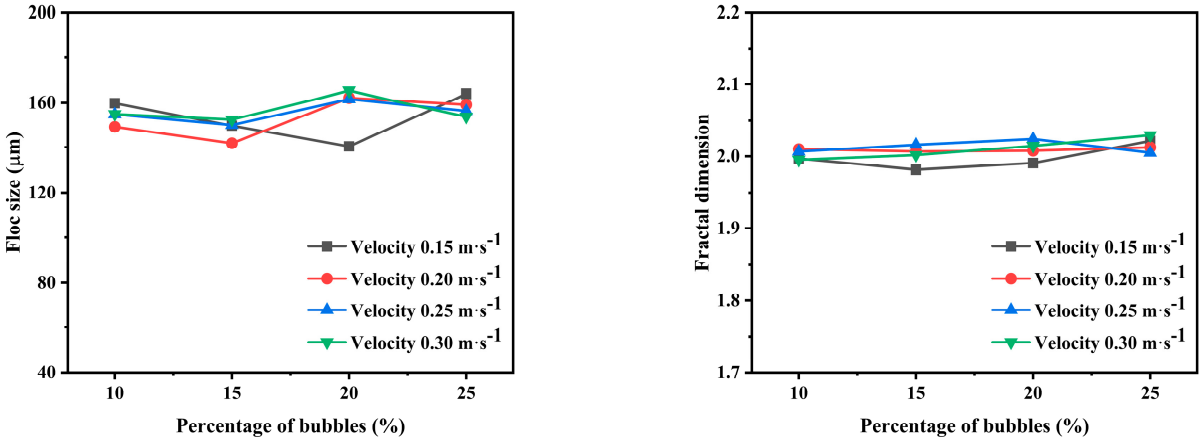


Figure 8. Effect of bubble water ratio on removal efficiency.

To explore how the increase in bubble water ratio affects removal efficiency, the shape and fractal dimension of flocs generated at different bubble water ratios and flow rates were statistically analyzed, as shown in Figure 9. In Figure 9A, the effect of different bubble water ratios on floc size is presented. It can be observed that as the bubble water ratio increases, the floc size fluctuates between 140 μm and 160 μm, showing no clear trend related to the bubble water ratio.



(**A**) (**B**)

Figure 9. Schematic of the effect of bubble water ratio on floc formation. (**A**) Effect of different bubble water ratios on floc size. (**B**) Effect of different bubble water ratios on floc fractal dimension.

Further comparison of the fractal dimension with bubble water ratio variations is shown in Figure 9B. Similar to the trend observed for floc size, the fractal dimension fluctuates around 2.0, with no significant effect from the increase in bubble water ratio on floc compactness [40].

Considering the removal efficiency, floc size, and fractal dimension variations together, it can be concluded that the relationship between bubbles and flocs is not solely determined by the bubbles being trapped within the flocs. A portion of the bubbles exists outside the flocs. The number of bubbles encapsulated by the flocs is more related to the time the bubbles participate in the floc formation rather than the total number of bubbles involved.

4. Conclusions

This study, based on a tubular coagulation reactor, used a uniform experimental design to investigate the effects of flow rate and dosage on removal efficiency in reactors with inner diameters of 12 mm and 6 mm under 20% bubble water conditions. The study also examined the impact of bubble inlet position and concentration on floc formation, the relationship between floc shape, and its impact on upward velocity. The conclusions are as follows:

(1) The removal efficiency has a logarithmic relationship with the floc's upward velocity. As the upward velocity increases from 0.1 mm·s^{-1} to 1.2 mm·s^{-1}, the removal efficiency rises from 38% to 90%. Once the upward velocity exceeds 0.7 mm·s^{-1}, the increase in removal efficiency levels off and converges at 90%.

(2) The upward velocity of the flocs is correlated with the floc's shape. Floc size has a linear correlation with upward velocity; as the floc size increases from 200 μm to 800 μm, the upward velocity increases from 0.4 mm·s^{-1} to 2.3 mm·s^{-1}. The fractal dimension of the flocs has an exponential correlation with upward velocity; as the fractal dimension increases from 1.93 to 2.02, the upward velocity decreases from 2.3 mm·s^{-1} to 0.4 mm·s^{-1}.

(3) The position of bubble introduction affects floc formation. As the bubble introduction position moves toward the outlet, the time for bubbles to participate in floc formation shortens. The generated floc size decreases from the 165 μm range to 160 μm, the fractal dimension of the flocs increases from 1.9 to 2.1, and the removal efficiency decreases from 70% to 60%.

(4) The amount of bubbles introduced does not significantly affect floc size and fractal dimension, but as the bubble proportion increases from 5% to 30%, the removal efficiency increases from 50% to 80%.

Author Contributions: Conceptualization, H.Z.; methodology, Y.Z.; software, Y.Z. and B.Y.; validation, Y.Z.; formal analysis, Y.Z. and Z.W.; resources, H.Z.; data curation, Y.Z.; writing—original draft preparation, Y.Z. and M.S.K.; writing—review and editing, C.W., X.Z., M.S.K. and H.Z.; visualization, Y.Z.; supervision, C.W., H.Z. and X.Z.; project administration, C.W., H.Z. and X.Z.; funding acquisition, C.W., H.Z., M.S.K. and X.Z. All authors have read and agreed to the published version of the manuscript.

Funding: The University Synergy Innovation Program of Anhui Province (GXXT-2023-104); Anhui Province Coal Clean Processing and Carbon Reduction Engineering Research Center Foundation (CCCE-2023001); China Postdoctoral Science Foundation (2020M671837); Anhui postdoctoral Foundation (2021A479).

Data Availability Statement: Data will be made available on request.

Conflicts of Interest: Author Zihao Wang is employed by the Bgrimm Technology Group. The remaining authors declare that the research was conducted in the absence of any commercial or financial relationships that could be construed as a potential conflict of interest.

References

1. Bak, M.P.; Kroeze, C.; Janssen, A.B.G.; Strokal, M. Modelling future coastal water pollution: Impacts of point sources, socio-economic developments & multiple pollutants. *Environ. Res. Lett.* **2024**, *19*, 064028.
2. Tu, T.; Li, L.; Li, W.; Zhang, S.; Zhong, H.; Ge, G.; Ma, Y.; Wu, L. Different patterns of bacterioplankton in response to inorganic and organic phosphorus inputs in freshwater lakes—A microcosmic study. *Water Res.* **2025**, *268*, 122645. [CrossRef] [PubMed]
3. Mohammed, V.; Arockiaraj, J. Unveiling the trifecta of cyanobacterial quorum sensing: LuxI, LuxR and LuxS as the intricate machinery for harmful algal bloom formation in freshwater ecosystems. *Sci. Total Environ.* **2024**, *924*, 171644. [CrossRef] [PubMed]
4. Vargas, P.P.; Castro, L.R.; Souza, C.A.D.; Rivera, A.L. Effects of the harmful algal bloom toxin, okadaic acid, on the mechanoreceptors of larval anchoveta (*Engraulis ringens*) under varying environmental conditions. *Front. Mar. Sci.* **2024**, *11*, 1446509.
5. Brooks, B.W. Deconvoluting the impacts of harmful algal blooms in multi-stressed systems. *Nat. Water* **2024**, *2*, 813–814. [CrossRef]
6. Piernas, A.B.M.; Badagian, N.; Brena, B.M.; Parada, A.P.; Reyes, J.F.G. Identification and occurrence of microcystins in freshwaters and fish from a eutrophic dam through LC-HRMS. *Sci. Total Environ.* **2025**, *959*, 178230. [CrossRef]
7. Alshahri, A.H.; Dehwah, A.H.A.; Winters, H.; Ghaffour, N.; Missimer, T.M. Evaluation of liquid ferrate role on controlling assimilable organic carbon (AOC) formation for seawater desalination pretreatment during harmful algal blooms. *Desalination Water Treat.* **2025**, *321*, 100940. [CrossRef]
8. Lv, S.; Zhang, L.; Zhang, L.; Liu, S.; Fan, W. Hydrogen-producing nanosilicon gel spheres for remediation of copper-polluted aquatic ecosystems: Oxidative stress mitigation and ecological recovery. *Chem. Eng. J.* **2025**, *504*, 159083. [CrossRef]
9. Wang, Y.; Niu, L.; Li, Y.; Zou, G.; Wu, J.; Zheng, J. Using modern coexistence theory to understand the distinct states of phytoplankton communities in a subtropical eutrophic river network. *Water Res.* **2025**, *274*, 123062. [CrossRef]
10. Deng, Y.; Yan, X.; Hou, M.; Yao, S. Reassessing the ecological effectiveness of ecological restoration programs: Evidence from a quasi-natural experiment in China. *Ecol. Eng.* **2025**, *212*, 107506. [CrossRef]
11. Yang, L.; Chen, Q.; Wei, J.; Fan, T.; Kong, L.; Long, T.; Zhang, S.; Deng, S. Response of microbial communities in aquifers with multiple organic solvent contamination: Implications for MNA remedy. *J. Hazard. Mater.* **2024**, *474*, 134798. [CrossRef] [PubMed]
12. McGuire, B.T.; Sanderson, M.P.; Smith, J.L.; Gobler, C.J. Clearance rates and toxin accumulation by North Atlantic bivalves during harmful algal blooms caused by the dinoflagellate, Dinophysis acuminata, in NY, USA, estuaries. *Harmful Algae* **2025**, *141*, 102745. [CrossRef] [PubMed]
13. Soudagar, M.E.M.; Kiong, T.S.; Jathar, L.; Ghazali, N.N.N.; Ramesh, S.; Awasarmol, U.; Ong, H.C. Perspectives on cultivation and harvesting technologies of microalgae, towards environmental sustainability and life cycle analysis. *Chemosphere* **2024**, *353*, 141540. [CrossRef] [PubMed]
14. Zhang, Y.; Ji, Y. Research on the application of interception engineering in the treatment of blue algae in South Taihu Lake. In *Energy Revolution and Chemical Research*; CRC Press: Boca Raton, FL, USA, 2022.
15. Aditya, L.; Vu, H.P.; Johir, M.A.H.; Mao, S.; Ansari, A.; Fu, Q.; Nghiem, L.D. Synthesizing cationic polymers and tuning their properties for microalgae harvesting. *Sci. Total Environ.* **2024**, *917*, 170423. [CrossRef]
16. Yin, Z.; Zhu, L.; Shi, X.; Gentili, F.G.; Nugroho, Y.K. Chitosan-β-cyclodextrin composite flocculants dual-drive for efficient microalgae harvesting: Structural evidences, dehydration process, E-DLVO model behavior and biomass utilization. *Sep. Purif. Technol.* **2024**, *339*, 126498. [CrossRef]
17. Staub, P.F.; Salomon, M.; Assoumani, A.; Zakar, A.B. *Multiyear and Seasonal Wide-Scale Indicators for French Surface Waters Contamination by WFD Substances. Environmental Science and Pollution Research*; Springer: Berlin/Heidelberg, Germany, 2024; pp. 1–83.
18. Kamaliya, S.N.; Jhala, Y.K.; Patel, H.K.; Kumar, D.; Sharmathy, V.; Vyas, R.V. Isolation and characterization of native microalgae with potential for phycoremediation of heavy metal contaminated water. *Phycologia* **2024**, *63*, 369–377. [CrossRef]
19. Li, J.; Mubashar, M.; Zulekha, R.; Xu, C.; Zhang, X. Applications of coagulation-sedimentation and ultrafiltration for the removal of nanoparticles from water. *Sep. Purif. Technol.* **2025**, *357*, 129920. [CrossRef]
20. Manhong, H.; Zheng, L.; Long-Fei, R.; Qianqian, W.; Jun, L.; Jialing, S.; Lijun, M. Robust mitigation of FO membrane fouling by coagulation-floatation process: Role of microbubbles. *Desalination* **2022**, *531*, 115693.
21. Craig, G.; Anthony, K.; Carleigh, S.; Sarah, P.; Eli, T.; Chad, S. Improvements in the reduction coagulation filtration process for hexavalent chromium treatment. *AWWA Water Sci.* **2023**, *5*, e1315.
22. Zhang, B.; Fang, Z.; Chen, J.; Wu, R.; Mao, B. Dual flocculation strategy with pH adjustment for cost-effective algae harvesting. *J. Water Process Eng.* **2024**, *59*, 105009. [CrossRef]
23. Zeng, G.; Zhang, R.; Liao, C.; Liang, D.; Wang, F.; Wang, Q.; Sun, D.; Lei, X. Efficacy and mechanism of Microcystis aeruginosa removal by activated carbon fiber/nanoscale zero-valent iron/nickel foam cathodic electrochemical system. *Environ. Pollut. Bioavailab.* **2024**, *36*, 2302499. [CrossRef]
24. Gonzalez-Torres, A.; Pivokonsky, M.; Henderson, R.K. The impact of cell morphology and algal organic matter on algal floc properties. *Water Res.* **2019**, *163*, 114887. [CrossRef] [PubMed]
25. Bismark, O.; Chunyang, X.; Yongping, C.; Yinpeng, Y.; Yan, Z. Experimental study on the effect of hydrodynamic conditions on flocculation and settling properties of fine-grain sediment. *Int. J. Sediment Res.* **2023**, *38*, 821–833.

26. Chen, Z.; Zhao, G.; Chen, B.; Chen, S.; Li, J.; Nong, Y. Influence of flocculation structure on time-dependent fluidity and rheological property of cement paste: Analytical models based on fractal theory. *Constr. Build. Mater.* **2024**, *455*, 139137. [CrossRef]
27. Karppinen, A.; Saarinen, T.; Salmela, J.; Laukkanen, A.; Nuopponen, M.; Seppälä, J. Flocculation of microfibrillated cellulose in shear flow. *Cellulose* **2012**, *19*, 1807–1819. [CrossRef]
28. Yin, W.; Xie, Y.; Yao, J.; Song, N.; Chen, K.; Yin, X. Study on the effect of flocculation morphology on the floatability of talc flocs and the adhesion mechanism with air bubbles. *Miner. Eng.* **2023**, *203*, 108317. [CrossRef]
29. Sun, Z.; Cao, H.; Shan, L.; Hu, X. Lattice-Boltzmann simulation of induced cavitation in protruding structure. *Numer. Heat Transf. Part A Appl.* **2019**, *76*, 465–478. [CrossRef]
30. Zhang, H.; Li, C.; Li, L.; Cheng, S.; Wang, P.; Sun, L.; Huang, J.; Zhang, X. Uncovering the optimal structural characteristics of flocs for microalgae flotation using Python-OpenCV. *J. Clean. Prod.* **2023**, *385*, 135748. [CrossRef]
31. Yao, M.; Ran, Z.; Chen, T.; Wu, Q.; Dong, X. Numerical simulation studies of agitating paddle dependence on characteristics of the flow field in the mechanical-continuous-flow-stirred reactor for flocculation. *Desalination Water Treat.* **2020**, *183*, 30–41. [CrossRef]
32. Haiyang, Z.; Lili, L.; Shaozhe, C.; Cheng, L.; Fangzhou, L.; Peizhong, W.; Lianjun, S.; Junbo, H.; Wen, Z.; Xuezhi, Z. Enhanced Microcystis Aeruginosa removal and novel flocculation mechanisms using a novel continuous co-coagulation flotation (CCF). *Sci. Total Environ.* **2022**, *857*, 159532.
33. Kubheka, N.P.; Shange, S.F.; Onwubu, S.C.; Deenadayalu, N.; Mdluli, P.S.; Mokhothu, T.H. ImageJ analysis for quantifying lead ion in environmental water using gold nanoparticles as a colorimetric probe. *J. Mol. Liq.* **2025**, *420*, 126804. [CrossRef]
34. Nie, X.; Yu, Z.; Li, Y.; Ouyang, S.; Wang, Z.; Wang, G. Simultaneous removal of cyanobacteria and algal organic matter (AOM) by $CaCO_3$ precipitation combined with Polyaluminum chloride (PACl) flocculation. *J. Water Process Eng.* **2024**, *66*, 105994. [CrossRef]
35. Liu, D.; Wu, M.; Li, X. A mechanism for the stable adhesion of bubbles and particles: The effect of particle surface properties. *J. Water Process Eng.* **2024**, *60*, 105154. [CrossRef]
36. Wang, Y.; Sun, W.; Ding, L.; Liu, W.; Tian, L.; Zhao, Y.; Zhang, M.; Wang, X. A study on the feasibility and mechanism of enhanced co-coagulation dissolved air flotation with chitosan-modified microbubbles. *J. Water Process Eng.* **2021**, *40*, 101847. [CrossRef]
37. Wang, H.; Chen, R.; Li, D.; Zhang, B.; Yan, X.; Ran, J.; Zhang, H. Probing the adaptability relationship between flow characteristics and mineral particles with different size and surface hydrophobicity. *Powder Technol.* **2025**, *452*, 120588. [CrossRef]
38. Zhou, R.; Li, X.; Li, D.; Wang, H.; Song, Z.; Yan, X.; Zhang, H. The Effect of Energy Input on Bubble-Particle Collision, Attachment, Detachment, and Collection Efficiencies in a Mechanical Flotation Cell. *Powder Technol.* **2025**, *in press*. [CrossRef]
39. Li, X.; Sun, Z.; Wang, H.; Wang, L.; Yan, X.; Zhang, H.; Ran, J.; Liu, J. Particle Motion under Turbulent Eddies: Inspiration for Fine Minerals Flotation. *Chem. Eng. Sci.* **2025**, *301*, 120754. [CrossRef]
40. Sun, Z.; Li, X.; Zhao, S.; Zhong, T.; Wang, L.; Yan, X.; Zhang, H. Enhanced Selective Recovery of Fine Minerals in Flotation by the Oscillatory Turbulence. *J. Environ. Chem. Eng.* **2025**, *13*, 115164. [CrossRef]

Disclaimer/Publisher's Note: The statements, opinions and data contained in all publications are solely those of the individual author(s) and contributor(s) and not of MDPI and/or the editor(s). MDPI and/or the editor(s) disclaim responsibility for any injury to people or property resulting from any ideas, methods, instructions or products referred to in the content.